Bulletin of the Seismological Society of America, Vol. 94, No. 4, pp. 1430–1440, August 2004

Seismic Velocity and Attenuation Structure of the East Rift Zone and South Flank of Kilauea Volcano, Hawaii

by S. Hansen, C. Thurber, M. Mandernach, F. Haslinger,* and C. Doran

Abstract It has been proposed that a deep magma body beneath the east rift zone (ERZ) of Kilauea volcano, Hawaii, must be present in order to explain the observed deformation of the south flank. From November 1999 to June 2000, 29 IRIS-PASSCAL three-component seismographs were operated across Kilauea's ERZ and south flank. Using local earthquakes recorded by these stations, supplemented with data from the Hawaiian Volcano Observatory stations, we investigated the deep structure of the ERZ and south flank through two approaches: seismic velocity tomography and seismic attenuation tomography. Results along two north-northwest–south-southeast profiles are examined. The western profile shows a low-velocity region beneath and south of the Hilina Pali, and earthquakes at depth are sandwiched between a high V_p/V_s, high Q zone and a low V_p/V_s, low Q zone. The velocity and attenuation differences are interpreted to reflect the contrast in material properties between the overlying volcanic pile and the underlying fluid-rich ocean sediments and fractured, altered ocean crust beneath the south flank thrust fault. The eastern profile shows an anomalous feature with low V_p, low V_p/V_s, high Q_p, and low Q_s at about 7 km depth beneath the ERZ. The low V_p/V_s ratio is inconsistent with the presence of partial melt. Instead, this anomaly is attributed to a trapped reservoir of CO_2. Our results do not support the existence of a sizable molten or partially molten body at depth beneath the ERZ. If the deep magma body exists, it must be relatively small. Based on synthetic resolution tests, an estimated limit on the maximum allowable cross-sectional size of the deep magma body is about 2 by 4 km.

Introduction

Historically, southern Hawaii has experienced a number of large-magnitude earthquakes, such as the M 7.9 Kau earthquake in 1868 and the M 7.2 Kalapana earthquake in 1975 (Lipman *et al.*, 1985). Although much has been learned about the structure of Kilauea over the past several decades, the process leading to such large earthquakes is still not well understood. Many have concluded that slip on low-angle (2°–8°) thrust faults at the volcano–ocean crust interface beneath southern Hawaii is at least partially responsible for such earthquakes. Geodetic studies have shown that the south flank is moving southward at rates on the order of 10 cm/yr (Delaney *et al.*, 1993; Owen *et al.*, 1995). However, modeling of the velocity gradients across Kilauea's rift zones has shown that fault slip alone cannot explain the observed deformation. Delaney *et al.* (1990) proposed that a deep magma body (DMB), at a depth of about 6–9 km beneath Kilauea's east rift zone (ERZ), may contribute to the ongoing deformation. In order to understand the behavior of Kilauea's south flank, it is essential to determine whether or not the hypothesized DMB exists.

In this study, we use two techniques to characterize the deep structure of the ERZ and to determine if the hypothesized DMB is present. The first approach, seismic velocity tomography, inverts *P*- and *S*-wave arrival times from local events to construct a 3D velocity model. Previous velocity tomography studies at Kilauea (Thurber, 1984; Rowan and Clayton, 1993; Okubo *et al.*, 1997; Dawson *et al.*, 1999; Haslinger *et al.*, 2001) have identified one or more low-velocity zones beneath the summit and/or rift zones, but no conclusive evidence of a low-velocity zone with the appropriate size and depth to correspond to the DMB has been detected. The second approach, seismic attenuation tomography, involves fitting *P*- and *S*-wave amplitude spectra for the attenuation parameter, t^*. The t^* data, along with the developed velocity model, are then used to solve for the quality factor (Q) structure. Since areas of magma accumulation have high attenuation (low Q) and low velocity, the combination of results from these two approaches should identify the DMB, if it exists.

*Present address: Prepatory Commission for the Comprehensive Nuclear-Test-Ban Treaty Organization, P.O. Box 1250, A-1400, Vienna, Austria.

Data

The data for this study were gathered from November 1999 to June 2000, across the ERZ and south flank of Kilauea volcano. A temporary network of 29 IRIS-PASSCAL seismographs, equipped with 1-Hz three-component geophones, was distributed along two roughly parallel profiles (Fig. 1). These profiles extended from the coast inland, trending south-southeast–north-northwest. One profile crossed the east rift near the Pauahi crater, and the other reached the rift near Makaopuhi crater. In addition, a 2D array of stations was deployed north of the rift. All of the stations had a sampling rate of 100 samples/sec, and events were defined by at least four triggered stations within a 10-sec time window. Data from the temporary array were combined with data from the permanent Hawaiian Volcano Observatory (HVO) stations, leading to a total of 5126 recorded events (Haslinger *et al.*, 2001).

From the original data set, 345 events were selected for use in the inversions based on their geographic distribution, hypocentral depth, and signal-to-noise (S/N) ratio. Most of the recorded earthquakes were crustal tectonic events, whose depths vary across the region. Most events within the ERZ are concentrated within a shallow layer at 2–4 km depth. In contrast, events south of the ERZ are concentrated in a deeper layer at 6–10 km depth. Events north of the ERZ are rare. Some deep mantle events (between about 30 and 40 km) were also recorded and included in the inversion.

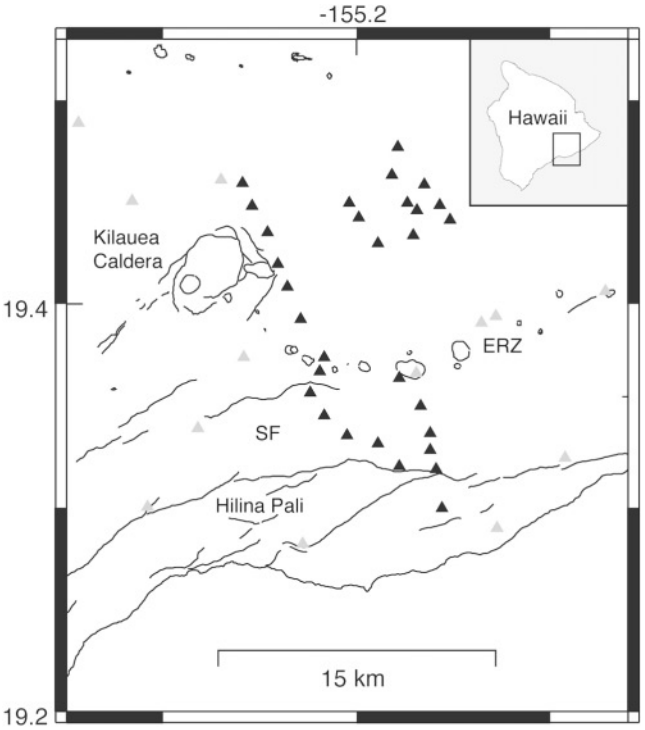

Figure 1. Map showing the locations of the permanent HVO stations (gray triangles) and the temporary PASSCAL stations (black triangles). SF, south flank, ERZ, east rift zone.

Methodology

Velocity Tomography

For the 345 selected events, 7433 *P*-wave arrivals and 5662 *S*-wave arrivals were determined. Preliminary locations for the earthquakes were taken from the HVO event catalog. The arrival times, pick weights, and preliminary locations were used in the inversion program simul2000 to solve simultaneously for the final earthquake locations and the 3D seismic velocity structure (Thurber, 1983; Thurber and Eberhart-Phillips, 1999).

The inversion program represents the subsurface velocity structure as a set of grid points and then interpolates the velocities between these points. Using an initial 1D model developed by Haslinger *et al.* (2001), the velocities at all the grid points and the locations of all the hypocenters are iteratively perturbed using a damped least-squares (DLS) approach. The estimated model parameters are improved by minimizing the weighted root mean square (rms) misfit between the calculated and observed arrival times as described by Thurber and Eberhart-Phillips (1999).

A series of tests was performed in order to determine the best grid spacing. The final model has two north-northwest–south-southeast planes of nodes, spaced 5 km apart, which allowed for analysis of two cross sections. Along each of these cross sections, the nodes in the horizontal, or north-northwest–south-southeast, direction are spaced 2 km apart on the south side of the model and 4 km apart on the north side of the model. In the vertical direction, the node spacing is 2 km between the surface and 11 km depth. The vertical spacing then increases from 5 to 15 km between 11 and 40 km depth. The variable gridding is useful since areas that have fewer rays passing through them can be represented by sparser gridding. This reduces the computation time and results in more uniform model resolution.

In addition to the node-spacing tests, a variety of damping tests were performed. For any inversion, there is a trade-off between the uncertainty and model resolution (Menke, 1989). As the resolution increases, so does the uncertainty. Therefore, a good damping parameter is one that leads to a compromise between a well-resolved yet highly uncertain model and a poorly resolved model with low uncertainty. Based on previous work done by Haslinger *et al.* (2001) as well as a thorough trade-off analysis, the final damping values chosen were 5 for V_p, 2 for V_p/V_s, and 10 for station damping.

Attenuation Tomography

For attenuation tomography modeling, the amplitude spectra can be related to the attenuation and source parameters using the following equation:

$$\ln(A(f)) = \ln(\Omega_0) - \ln(1 + (f/f_c)^{\gamma}) + (-\pi f t^*), \quad (1)$$

where $A(f)$ is the amplitude at a given frequency f, f_c is the corner frequency, Ω_0 is the amplitude asymptote at zero frequency, γ is the source spectral fall-off, and t^* is the attenuation parameter (Lees and Lindley, 1994). It should be noted that for a given event, the value of f_c is the same for all stations. As written, this equation has four free parameters (namely, t^*, Ω_0, f_c, and γ). However, we cannot solve for this many variables and get a unique, best-fit solution since there are many possible combinations that will produce similar fits. Usually, an ω^{-2} or Brune source model is assumed, in which the spectral amplitudes fall off as ω^{-2} above the corner frequency. Using this assumption, the value of γ can be set to 2, leaving the remaining three parameters to be solved for (Al-Shukri and Mitchell, 1990).

The unknown parameters are determined using the Levenberg–Marquardt or iterative DLS method. Initial guesses of the three unknown parameters, t^*, Ω_0, and f_c, are made for each record, and derivatives of equation (1) with respect to each of the unknown parameters are used to construct a Jacobian matrix (**G**). Using this matrix and the residuals between the observed and calculated amplitude values (r), the model is perturbed using the following equation until a convergent solution is found (Menke, 1989):

$$\Delta m = [\mathbf{G}^T\mathbf{G} + \varepsilon^2\mathbf{I}]^{-1}\mathbf{G}^T r. \quad (2)$$

The value of ε, which is the damping parameter, can be varied to improve the stability of the solution while minimizing the number of iterations.

Once the t^* values have been determined, they can then be inverted to determine the Q structure. The equation relating these parameters is as follows:

$$t^* = \int_{\text{raypath}} [1/Q(x,y,z) * 1/V(x,y,z)]\mathrm{d}r, \quad (3)$$

where $V(x,y,z)$ is the velocity structure (Haberland and Rietbrock, 2001). This approach can be used for both P and S waves. The Q structure is represented on the same grid as the velocity structure, and since the event locations and velocity model are fixed in the attenuation inversions, the same ray paths are used for both the velocity and attenuation models.

Estimating Path Attenuation (t*). The best results were obtained with amplitude spectra determined for a 128-sample window around the seismic-wave arrivals. Following Rietbrock (2001), the noise spectrum was calculated from a section of the record just prior to the arrival. For S waves, the noise window was placed in the late P-wave coda. For a record to be used, the amplitude of the data spectrum had to be at least 3 times greater than the noise spectrum over a continuous frequency range of at least 10 Hz. If the S/N threshold could not be reached or if the range was too short, then the trace was not used in the inversion.

The actual range of frequencies fit was determined by the S/N ratio limits. At the extremes, frequencies below the natural frequency of the geophones, 1 Hz, were not used, and the highest frequency for fitting was 40 Hz. However, in general, the lower and upper frequency limits are where the S/N ratio climbs above and falls below the specified threshold, respectively. In addition, at least four records per event were required to use an event in the inversion.

Initial guesses of the unknown parameters were made for each station. The initial values of t^* and f_c were set to 0.05 sec and 10 Hz, respectively. The initial value of Ω_0 was the average amplitude between 1 and 5 Hz. These initial guesses, along with the observed data, were used in the inversion subroutine. The iterative DLS approach simultaneously solves for the unknown parameters at each station. Up to 15 iterations of the loop are allowed.

This analysis was performed for both P- and S-wave spectra. A total of 330 events meeting the selection criteria were processed with the t^* fitting code using the vertical components and the P-wave window, and a total of 341 events were processed using the horizontal components and the S-wave window. This resulted in 3997 estimated t^* parameters for P-wave spectra and 4347 for S-wave spectra. Figures 2 and 3 show examples of both P- and S-wave spectra that were fit using this approach. The computed attenuation parameters are assigned quality weights based on the rms difference between the observed and computed amplitude values (Eberhart-Phillips and Chadwick, 2002).

Solving for Q *Structure.* As with the velocity tomography, the simul2000 inversion program was used to invert the t^* values and solve for the Q structure. Given a set of t^* values and a 3D velocity model, the Q structure can be determined using equation (3). To solve for the Q_p structure, the V_p model and the t^* values from the vertical components are used. Similarly, to solve for the Q_s structure, the V_s model and the t^* values from the horizontal components are used.

As stated previously, the same node spacing that was used for the velocity tomography model was also used for both the attenuation tomography models. The final hypocenter locations were taken from the velocity tomography results as well. For both the Q_p and Q_s models, a uniform Q was used as the initial value. Trial inversions were carried out using a range of initial values, and based on those results, the initial Q values chosen were 150 for Q_p and 100 for Q_s. Different damping parameters were also examined to find the best compromise between model uncertainty and resolution. For the final Q_p and Q_s models, a damping value of 0.01 was chosen.

Results

Relocated Events

The final earthquake locations are determined as part of solving for the 3D velocity structure. Figure 4 shows both the original event locations from the HVO and the new locations determined by the inversion. In map view, the initial and final epicenters are similar in areas where good coverage

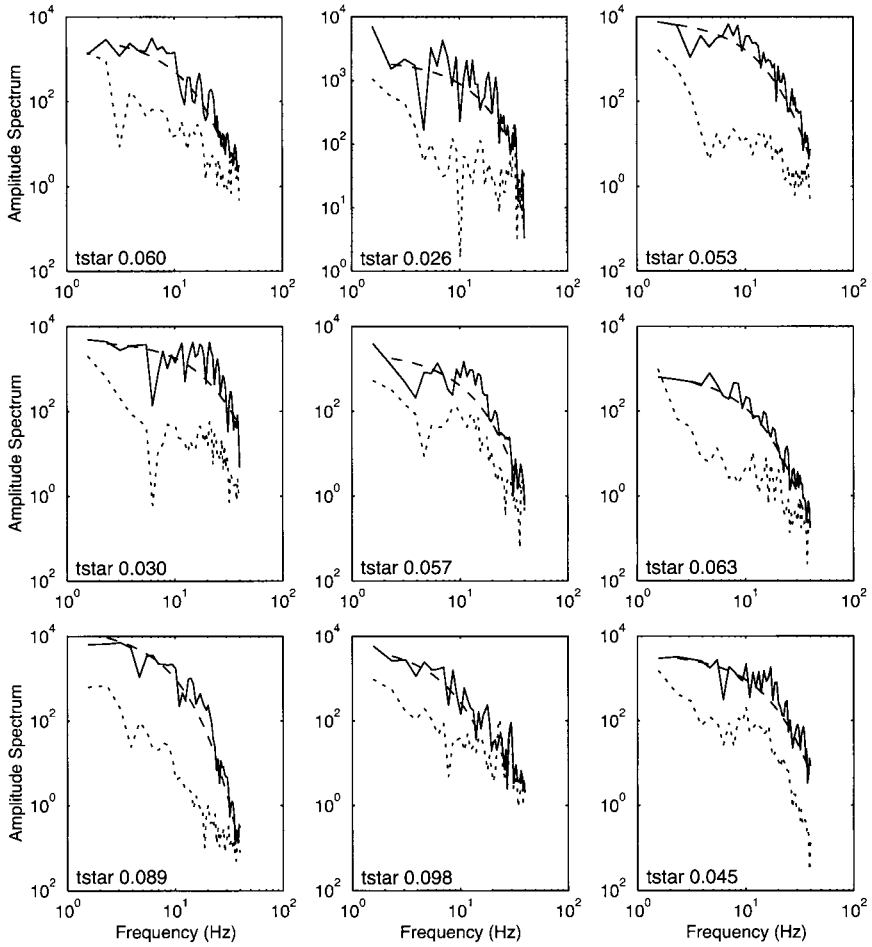

Figure 2. Examples of *P*-wave spectra fit by the *t** inversion code. The solid lines are the observed data spectra, and the dotted lines are the observed noise spectra. The dashed lines are the calculated fits to the spectra. The corresponding *t** values are listed.

is supplied by the HVO stations. However, where the HVO station coverage is poor, the final epicenters are significantly different from the initial locations. For example, many of the relocated south flank event epicenters have been shifted to the south. This is probably due to the sparse HVO coverage north of the ERZ.

In cross section, our results show far less scatter than the HVO locations; the events collapse to form relatively tight clusters at two main depths. The shallow cluster is at a depth of about 2–3.5 km, corresponding to events within the ERZ. The deeper cluster is at a depth of about 7–9 km and defines the thrust fault beneath the south flank. In contrast, the mantle events are more widely scattered.

Velocity Tomography

The tomography results are shown along the same two north-northwest–south-southeast profiles, labeled AA′ and BB′, in Figure 4. The AA′ profile passes along the east side of Kilauea's summit. The BB′ profile runs parallel to the AA′ profile but is 5 km further east. It is roughly perpendicular to the ERZ and crosses the rift zone near the Makaopuhi crater. For reference, the coordinate origin is marked by a small cross on Figure 4.

Along the AA′ profile, the most noticeable features on the V_p plot (Fig. 5a) are the high-velocity core of the volcano (~7 km/sec) and the low-velocity area (~5.5 km/sec) at the south end of the profile. This low V_p region underlies the Hilina Pali, and similar low V_p observations in this area have been made in previous studies (Rowan and Clayton, 1993; Okubo *et al.*, 1997; Haslinger *et al.*, 2001). The deep patch of seismicity, between 7 and 9 km depth, is also located beneath the Hilina Pali. The V_p/V_s plot (Fig. 5b) indicates that these events are sandwiched between a deeper high V_p/V_s area (~1.9) and a shallower low V_p/V_s area (~1.7).

Along the BB′ profile, there is a low V_p region centered at 7 km depth between −5 and 0 km (Fig. 6a). This region is north of and at approximately the same depth as the concentrated cluster of events, and it is located in approximately the same position as the hypothesized DMB (Delaney *et al.*, 1990). If this were an area of partial melt, *S*-wave velocities should be more strongly reduced than *P*-wave velocities, leading to a high V_p/V_s ratio. However, when the V_p/V_s plot

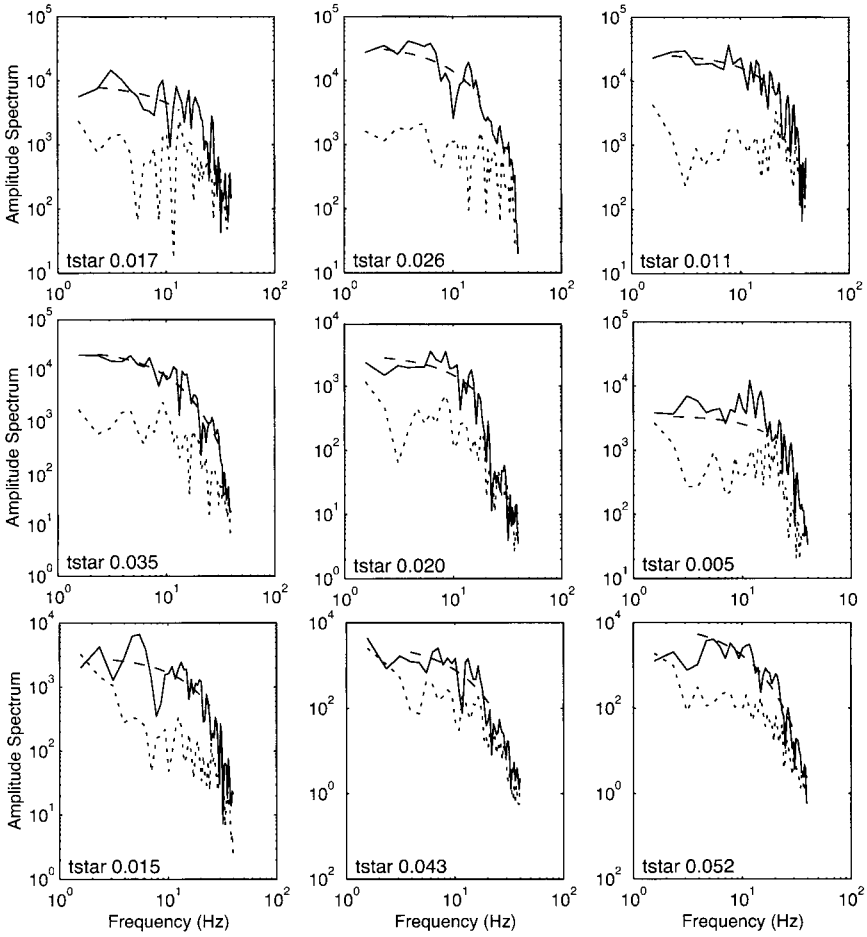

Figure 3. Examples of *S*-wave spectra fit by the *t** inversion code. The solid lines are the observed data spectra, and the dotted lines are the observed noise spectra. The dashed lines are the calculated fits to the spectra. The corresponding *t** values are listed.

is examined (Fig. 6b), we see that this area has a low V_p/V_s ratio (~1.7). Therefore, these results do not support the presence of a large DMB.

The final velocity model has a variance reduction of 59%. Figures 7 and 8 show contour plots of the resolution for V_p and V_p/V_s along the north-northwest–south-southeast profiles AA′ and BB′, respectively. The contours indicate the diagonal elements of the resolution matrix, where values closer to 1.0 indicate better resolution (Menke, 1989). Along both profiles, the model is well resolved at horizontal distances from about −10 to 10 km and to a depth of 10 km. Resolution values in this area vary from about 0.1 to 0.7. The average number of ray paths that correspond to these resolution values are 4300 and 11,500, respectively. Past 10 km depth, the resolution significantly worsens. Therefore, while the model depth extent is 40 km, only the well-resolved, upper portions of the models are described and presented in the attached figures.

Attenuation Tomography

Along the AA′ profile, the Q_p plot (Fig. 9a) illustrates a general increase of Q_p with depth, which is most likely caused by crack closure due to increasing confining pressure (Tompkins and Christensen, 1999). The deep patch of seismicity (7–9 km depth) is located between a shallower high Q_p area (>250) and a deeper low Q_p area (<150). On the Q_s plot (Fig. 9b), the area near these clustered events shows a similar contrast in quality values.

Along the BB′ profile, there is a high Q_p anomaly (~250) centered at 7 km depth between −5 and 0 km (Fig. 10a). This is the same position as the low V_p, low V_p/V_s feature seen in the velocity model. On the Q_s plot (Fig. 10b), this same region is marked by a low Q_s value (~100). In addition, there is a high Q_s anomaly (~250) near the surface at a horizontal distance of 5 km. However, when the damping tests were performed, it was observed that this feature would disappear and reappear as the damping values were changed. Therefore, this anomaly is not a robust feature and is instead interpreted to be an artifact.

The final Q_p model has a variance reduction of 48%, while the final Q_s model has a variance reduction of 47%. Figures 11 and 12 show contour plots of the resolution for Q_p and Q_s along the AA′ and BB′ profiles. While the attenuation model is not as well resolved as the velocity model,

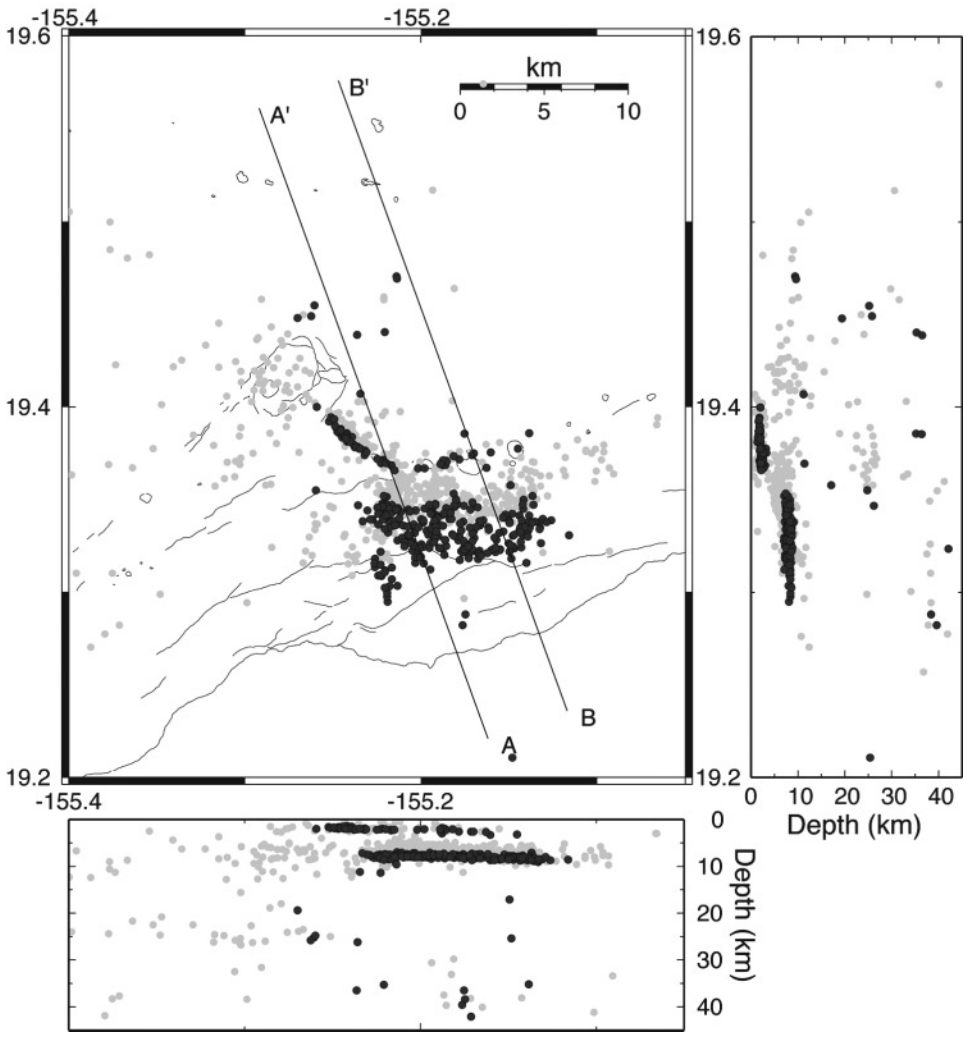

Figure 4. Map view and depth sections of selected seismicity recorded between November 1999 and June 2000. The gray dots denote the initial HVO locations, while the black dots denote the locations determined by the simul2000 inversion. Positions of the north-northwest–south-southeast profiles, AA′ and BB′, are also shown.

we still have fairly good resolution at horizontal distances from −8 to 6 km and to a depth of 7 km. Again, only the well-resolved, upper portions of the models are described and presented.

Discussion

AA′ Profile

When the velocity and attenuation models are compared, one can see that the deep patch of seismicity (7–9 km depth) is associated with a variety of changes. This concentrated patch of events defines the low-angle thrust fault beneath Kilauea's south flank. The thrust fault is presumed to have developed here due to a weak layer of ocean sediments beneath the volcanic pile, and these sediments lie below the fault plane. The sediments and underlying ocean crust are expected to have high porosity and crack density, respectively, and can be expected to have a decreased velocity and increased attenuation (Tsumura *et al.*, 1996). Theoretical and empirical studies have shown that increased fracturing and crack density leads to an increase in attenuation (O'Connell and Budiansky, 1977; Peacock *et al.*, 1994). The area beneath the patch of earthquakes has a relatively low V_p, as well as low Q_p and low Q_s. Therefore, the model results in this area reflect the weak layer of ocean sediments and the fractured, altered ocean crust underlying the thrust fault.

In addition, there is a change in the V_p/V_s ratio around this patch of seismicity. The low and high V_p/V_s areas correlate, respectively, with the changes from high to low Q_p and Q_s. Changes in the V_p/V_s ratio similar to those observed here have been seen along sections of the San Andreas fault, where the increased V_p/V_s ratio was attributed to the presence of pore fluids (Thurber *et al.*, 1997). Studies have

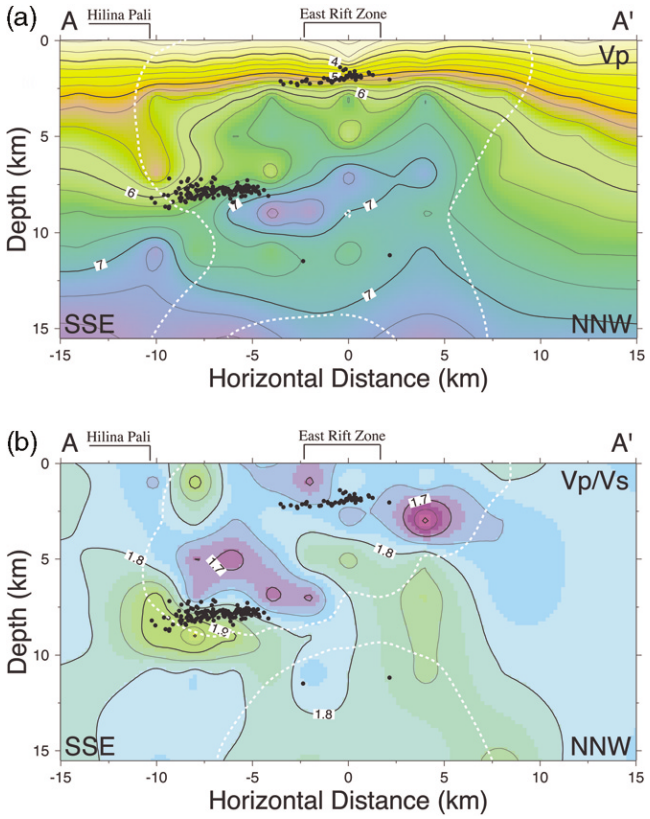

Figure 5. (a) *P* velocity structure and (b) V_p/V_s structure along the AA′ profile. Earthquakes within 3 km perpendicular distance of the profile are shown (black dots). Thin black lines denote velocity contours (every 0.25 km/sec), and 0 km depth indicates sea level. Dashed white lines indicate the area with resolution matrix diagonal elements above 0.2.

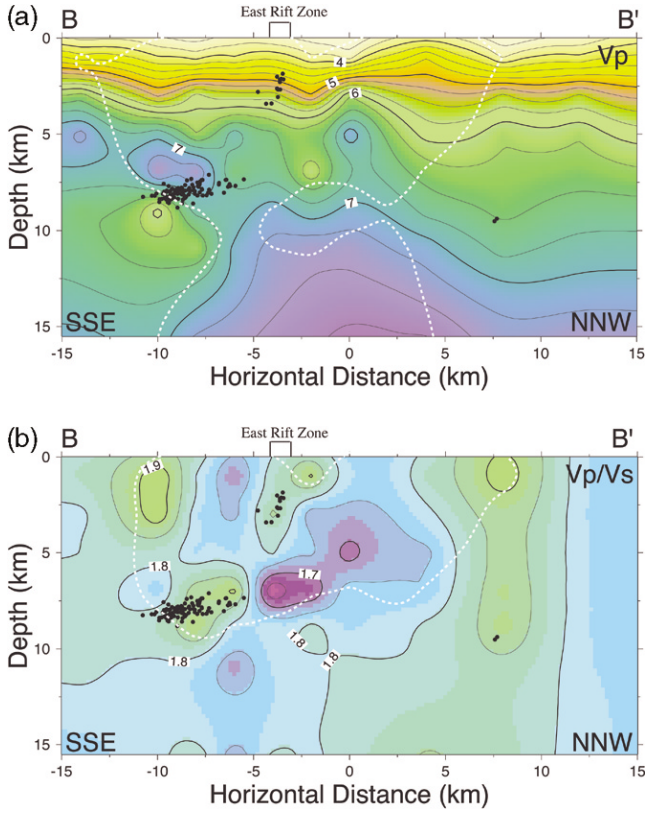

Figure 6. (a) *P* velocity structure and (b) V_p/V_s structure along the BB′ profile. Earthquakes within 3 km perpendicular distance to the profile are shown (black dots). Thin black lines denote velocity contours (every 0.25 km/sec), and 0 km depth indicates sea level. Dashed white lines indicate the area with resolution matrix diagonal elements above 0.2.

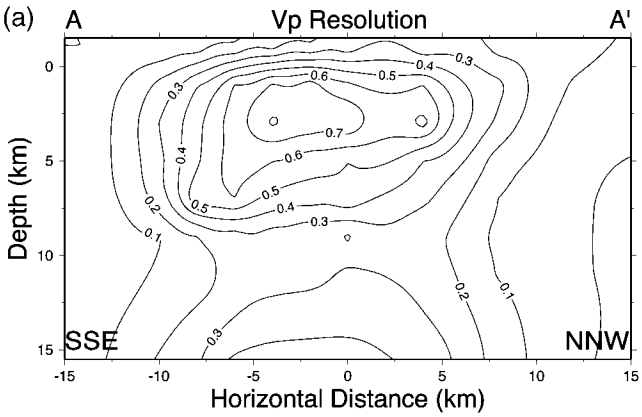

Figure 7. V_p and V_p/V_s resolution of the 3D inversion along the AA′ profile. The contours indicate the diagonal elements of the resolution matrix.

shown that increased pore fluid pressure leads to increased *P*-wave attenuation (Winkler and Nur, 1979; Tompkins and Christensen, 1999), as well as increased *S*-wave attenuation (Winkler and Nur, 1982). Therefore, the high V_p/V_s ratio and high attenuation in the area beneath the earthquakes may also reflect the presence of pore fluids. This agrees with suggestions made in previous studies that pore fluid pressure may contribute to faulting and regions of reduced strength beneath the south flank (Dieterich, 1988; Ryan, 1988; Thurber and Gripp, 1988).

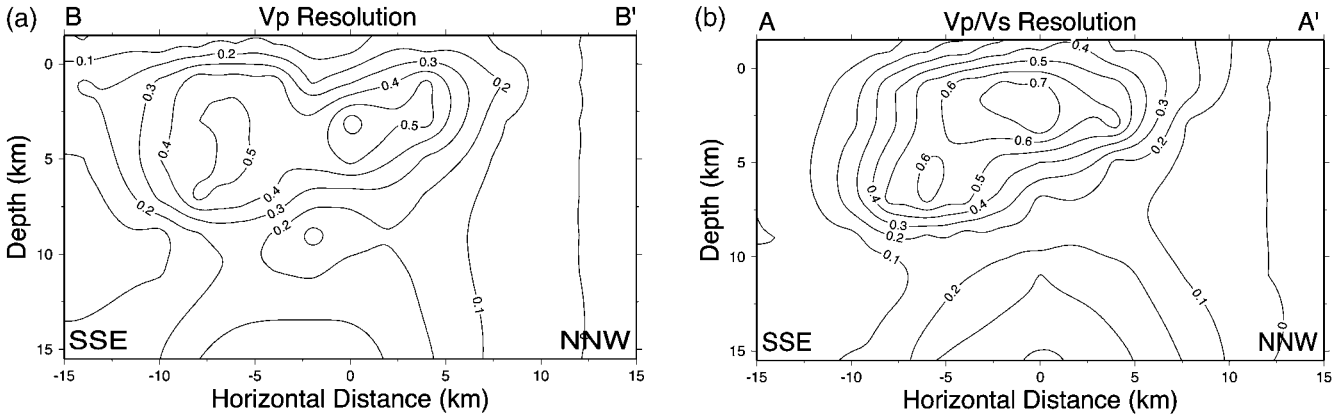

Figure 8. V_p and V_p/V_s resolution of the 3D inversion along the BB′ profile. The contours indicate the diagonal elements of the resolution matrix.

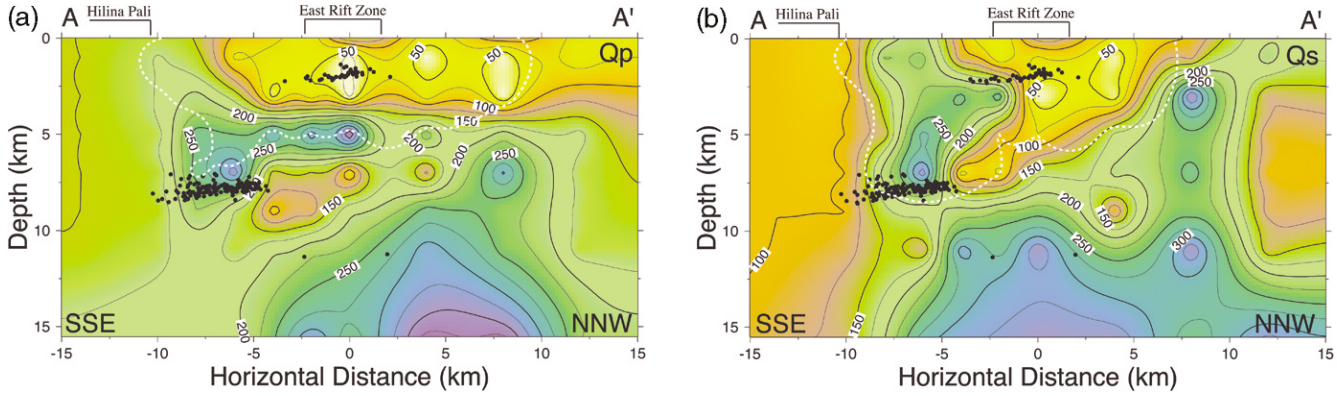

Figure 9. (a) Q_p structure and (b) Q_s structure along the AA′ profile. Earthquakes within 3 km perpendicular distance to the profile are shown (black dots). Thin black lines denote quality value contours (at 25 intervals), and 0 km depth indicates sea level. Dashed white lines indicate the area with resolution matrix diagonal elements above 0.1. Since the number of events meeting the selection criteria were different for *P* and *S* waves, the earthquakes in panels a and b differ slightly.

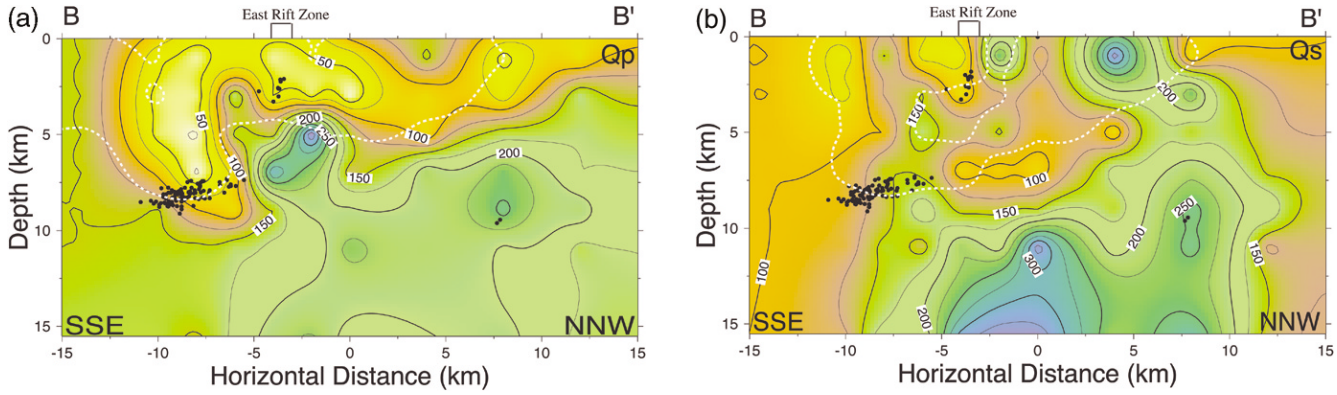

Figure 10. Q_p structure and (b) Q_s structure along the BB′ profile. Earthquakes within 3 km perpendicular distance to the profile are shown (black dots). Thin black lines denote quality value contours (at 25 intervals), and 0 km depth indicates sea level. Dashed white lines indicate the area with resolution matrix diagonal elements above 0.1. Again, the earthquakes in panels a and b differ slightly due to the difference in events meeting the selection criteria.

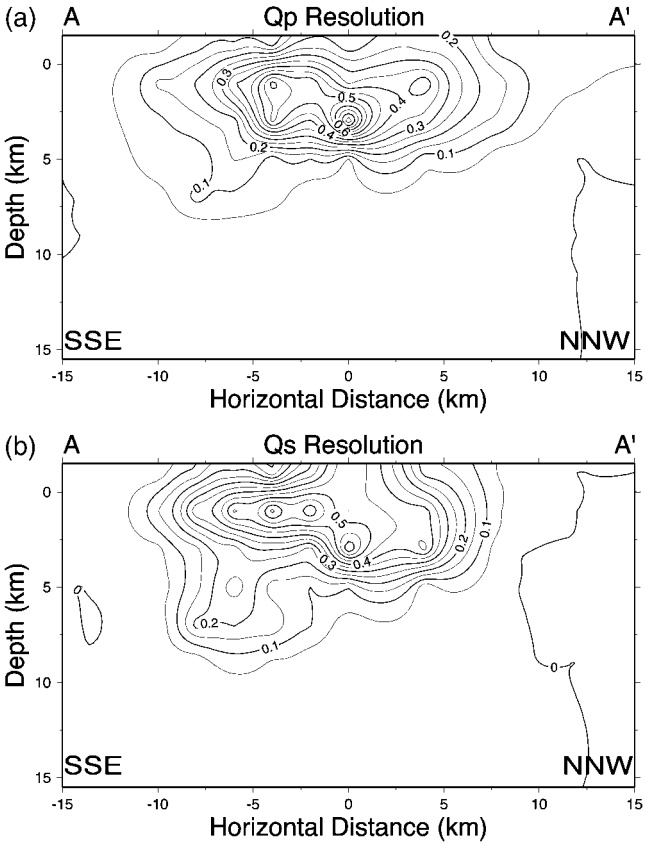

Figure 11. Q_p and Q_s resolution of the 3D inversion along the AA′ profile. The contours indicate the diagonal elements of the resolution matrix.

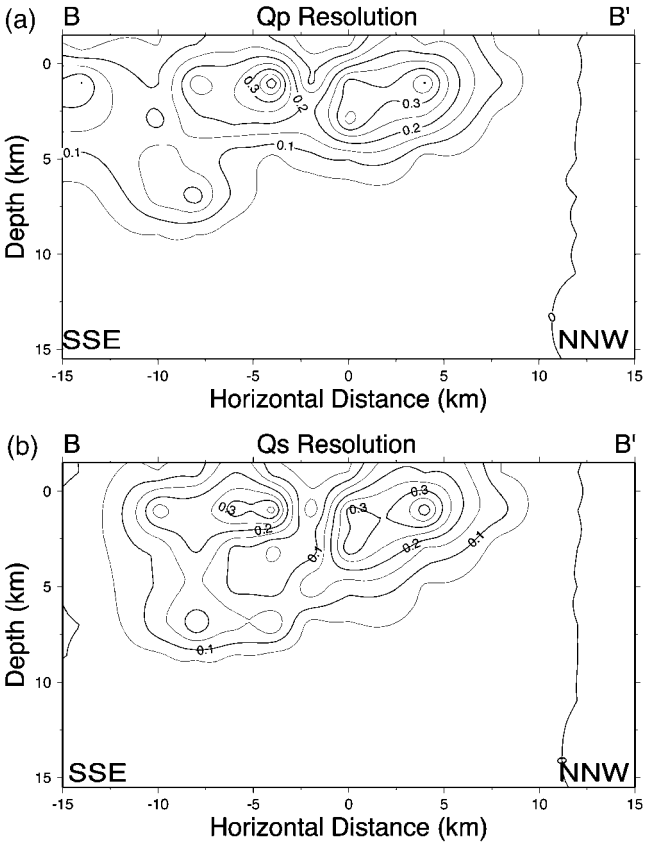

Figure 12. Q_p and Q_s resolution of the 3D inversion along the BB′ profile. The contours indicate the diagonal elements of the resolution matrix.

BB′ Profile

The main feature of interest along the BB′ profile is an area of low *P*-wave velocity, low V_p/V_s ratio, high Q_p, and low Q_s, centered at 7 km depth between −5 and 0 km. The low V_p/V_s ratio observed does not support the presence of partial melt. We suggest that this low V_p, low V_p/V_s anomaly is due to gas-filled porosity. The presence of gas would decrease the bulk modulus of the rock, leading to a decrease in the *P*-wave velocity. However, this would not significantly affect the *S*-wave velocity, resulting in a low V_p/V_s ratio.

In basaltic magma, CO_2 is the most common volatile. The CO_2 content of the parental magma at Kilauea is unknown, but model results estimate initial CO_2 values between 0.32 (Greenland *et al.*, 1985) and 0.65 wt % (Gerlach and Graeber, 1985). At depth, the magma is saturated in CO_2, but as the magma rises, the decrease in confining pressure causes the magma to decompress and CO_2 exsolves. However, according to the closed system degassing stage, the gas bubbles cannot ascend to the surface faster than the magma, so the bulk density of the magma is decreased as the magma approaches the surface (Gerlach and Taylor, 1990). As the magma cools and solidifies, most of the CO_2 would be exsolved, but without connected porosity the gas would not be able to escape to the surface and would be trapped. A modest amount of CO_2-filled porosity could explain the observed low V_p, low V_p/V_s anomalies of about −5%, comparable to the results of Julian *et al.* (1998) for Mammoth Mountain, California.

A trapped reservoir of CO_2 could also explain the observed attenuation. Case studies have shown an increase in *S*-wave attenuation associated with the presence of gas (Sengupta and Rendleman, 1989). The anomalous high Q_p value may also be attributed to the presence of trapped CO_2. Laboratory experiments have shown that at pressures below the saturation pressure (in this case corresponding to a depth less than 28 km; Gerlach and Taylor [1990]), the presence of gas can lead to a decrease in both the *P*-wave velocity and the *P*-wave attenuation (Ito *et al.*, 1979; Spencer, 1979).

The features observed at depth beneath the ERZ in both the velocity and attenuation models are best explained by a region of trapped CO_2. No evidence supporting the presence of a large DMB beneath the ERZ has been observed. If an area of partial melt exists beneath the rift zone, it must be relatively small. Synthetic tests were carried out to assess the minimum size of an anomaly located at depth beneath the ERZ that would be detected reliably. We imbedded one-

and two-node V_p, V_s, Q_p, and Q_s anomalies (one at a time, with 2-km gridding) within models taken from our actual solutions and created synthetic data matching the exact set of observations used with the actual data. We found that a one-node V_p anomaly could be detected, whereas only the two-node anomalies could be detected for V_s, Q_p, and Q_s. Thus a deep magma body larger than 2 by 4 km in cross-sectional size would be reliably detected with our inversion.

Conclusions

Combining velocity and attenuation tomography has allowed us to gain greater insight into the structure beneath Kilauea's ERZ and south flank. Figure 13 shows sketches of the interpreted features along each profile of our tomography model. Below the Hilina Pali, the weak sediment layer beneath the fault plane and the possible presence of pore fluids are reflected in the changing V_p/V_s ratio, as well as the changing quality factors. Beneath the ERZ, an anomalous feature showing low V_p, low V_p/V_s, high Q_p, and low Q_s was identified. Although this feature is located in approximately the same position as the proposed DMB, the low V_p/V_s ratio does not support the hypothesis that this area contains substantial melt. Instead, an area of CO_2-filled porosity best explains the observed features. Since no evidence of partial melt beneath the ERZ has been found, any existing DMB must be relatively small. Resolution tests limit the maximum size of the DMB to about 2 by 4 km in cross section.

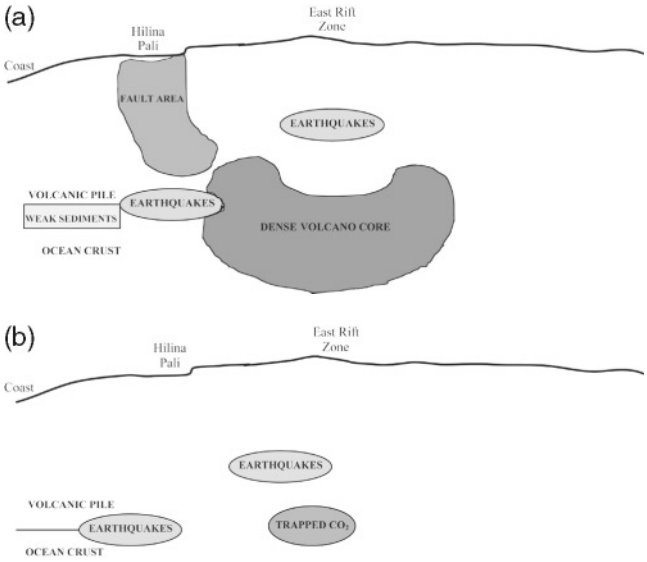

Figure 13. Sketch showing the interpreted structures along the (a) AA′ and (b) BB′ profiles. In AA′, note the shallow and deep clusters of earthquakes, the dense volcanic core, the weak sediments below the thrust fault, and the faulted region below Hilina Pali. In BB′, note the shallow and deep clusters of earthquakes and the interpreted trapped CO_2 reservoir beneath the east rift zone.

Acknowledgments

Our thanks to the KERZ field crew for all of their hard work: from UW–Madison, Ben Abernathy, Astrid Haslinger, Neal Lord, Lee Powell, Chad Trabant, and Mike Tryggestad; from the PASSCAL Instrument Center, Mary Templeton. Additional help from Bill Unger, Bill Lutter, Paul Okubo, and Renate Hartog is appreciated. We thank Phil Dawson and Dapeng Zhao for constructive reviews. The instruments used in the field program were provided by the PASSCAL facility of the IRIS through the PASSCAL Instrument Center at New Mexico Tech. Data collected during this experiment are available through the IRIS Data Management Center. The facilities of the IRIS Consortium are supported by the National Science Foundation under Cooperative Agreement EAR-0004370. This material is based upon work supported by the National Science Foundation under Grant Number EAR 9814359.

References

Al-Shurki, H., and B. Mitchell (1990). Three-dimensional attenuation structure in and around the New Madrid seismic zone, *Bull. Seism. Soc. Am.* **80,** 615–632.

Dawson, P. B., B. A. Chouet, P. G. Okubo, A. Villasenor, and H. M. Benz (1999). Three-dimensional velocity structure of the Kilauea caldera, Hawaii, *Geophys. Res. Lett.* **26,** 2805–2808.

Delaney, P., R. Fiske, A. Miklius, A. Okamura, and M. Sako (1990). Deep magma body beneath the summit and rift zones of Kilauea volcano, Hawaii, *Science* **247,** 1311–1316.

Delaney, P., A. Miklius, T. Arnadottir, A. Okamura, and M. Sako (1993). Motion of Kilauea volcano during sustained eruption from the Puu Oo and Kupaianaha vents, 1983–1991, *J. Geophys. Res.* **98,** 17,801–17,820.

Dieterich, J. (1988). Growth and persistence of Hawaiian volcanic rift zones, *J. Geophys. Res.* **93,** 4258–4270.

Eberhart-Phillips, D., and M. Chadwick (2002). Three-dimensional attenuation model of the shallow Hikurangi subduction zone in the Raukumara Peninsula, New Zeland, *J. Geophys. Res.* **107,** no. B2 (ESE3), 1–15.

Gerlach, T., and E. Graeber (1985). Volatile budget of Kilauea volcano, *Nature* **313,** 273–277.

Gerlach, T., and B. Taylor (1990). Carbon isotope constraints on degassing of carbon dioxide from Kilauea volcano, *Geochim. Cosmochim. Acta* **54,** 2051–2058.

Greenland, L. P., W. I. Rose, and J. B. Stokes (1985). An estimate of gas emissions and magmatic gas content from Kilauea volcano, *Geochim. Cosmochim. Acta* **49,** 125–129.

Haberland, C., and A. Rietbrock (2001). Attenuation tomography in the western central Andes: a detailed insight into the structure of a magmatic arc, *J. Geophys. Res.* **106,** 11,151–11,167.

Haslinger, F., C. Thurber, M. Mandernach, and P. Okubo (2001). Tomographic image of *P*-velocity structure beneath Kilauea's east rift zone and south flank: seismic evidence for a deep magma body, *Geophys. Res. Lett.* **28,** no. 2, 375–378.

Ito, H., J. DeVilbiss, and A. Nur (1979). Compressional and shear waves in saturated rock during water–steam transition, *J. Geophys. Res.* **84,** 4731–4735.

Julian, B. R., A. M. Pitt, and G. R. Foulger (1998). Seismic image of a CO_2 reservoir beneath a seismically active volcano, *Geophys. J. Int.* **133,** F7–F10.

Lees, J. M., and G. T. Lindley (1994). Three-dimensional attenuation tomography at Loma Prieta: inversion of t^* for Q, *J. Geophys. Res.* **99,** 6843–6863.

Lipman, P., J. Lockwood, R. Okamura, D. Swanson, and K. Yamashita (1985). Ground deformation associated with the 1975 magnitude-7.2 earthquake and resulting changes in activity of Kilauea volcano, Hawaii, *U.S. Geol. Surv. Profess. Pap. 1276*, 1–45.

Menke, W. (1989). *Geophysical Data Analysis: Discrete Inverse Theory*, Academic, New York.

O'Connell, R. J., and B. Budiansky (1977). Viscoelastic properties of fluid-saturated cracked solids, *J. Geophys. Res.* **82,** 5719–5735.

Okubo, P., H. Benz, and B. Chouet (1997). Imaging the crustal magma sources beneath Mauna Loa and Kilauea volcanoes, Hawaii, *Geology* **25,** 867–870.

Owen, S., P. Segall, J. Freymueller, R. Denlinger, T. Arnadottir, M. Sako, and R. Burgmann (1995). Rapid deformation of the south flank of Kilauea volcano, Hawaii, *Science* **267,** 1328–1332.

Peacock, S., C. McCann, J. Sothcott, and T. R. Astin (1994). Experimental measurements of seismic attenuation in microfractured sedimentary rock, *Geophysics* **59,** 1342–1351.

Rietbrock, A. (2001). *P* wave attenuation structure in the fault area of the 1995 Kobe earthquake, *J. Geophys. Res.* **106,** no. B3, 4141–4154.

Rowan, L., and R. Clayton (1993). The three-dimensional structure of Kilauea volcano, Hawaii, from traveltime tomography, *J. Geophys. Res.* **98,** 4355–4375.

Ryan, M. (1988). The mechanics and three-dimensional internal structure of active magmatic systems: Kilauea volcano, Hawaii, *J. Geophys. Res. 93*, 4213–4248.

Sengupta, M. K., and C. A. Rendleman (1989). Case study: the importance of gas leakage in interpreting amplitude-versus-offset (AVO) analysis, *Soc. Explor. Geophys. Abstracts* **59,** 848–850.

Spencer, J. (1979). Bulk and shear attenuation in Berea sandstone: the effects of pore fluids, *J. Geophys. Res.* **84,** 7521–7523.

Thurber, C. (1983). Earthquake locations and three-dimensional crustal structure in the Coyote Lake area, central California, *J. Geophys. Res.* **88,** 8226–8236.

Thurber, C. H. (1984). Seismic detection of the summit magma complex of Kilauea volcano, Hawaii, *Science* **223,** 165–167.

Thurber, C., and D. Eberhart-Phillips (1999). Local earthquake tomography with flexible gridding, *Comp. Geosci.* **25,** 809–818.

Thurber, C., and A. Gripp (1988). Flexure and seismicity beneath the south flank of Kilauea volcano and tectonic implications, *J. Geophys. Res.* **93,** 4271–4288.

Thurber, C., S. Roecker, W. Ellsworth, Y. Chen, W. Lutter, and R. Sessions (1997). Two-dimensional seismic image of the San Andreas fault in the northern Gabilan Range, central California: evidence for fluids in the fault zone, *Geophys. Res. Lett.* **24,** 1591–1594.

Tompkins, M. J., and N. I. Christensen (1999). Effects of pore pressure on compressional wave attenuation in a young oceanic basalt, *Geophys. Res. Lett.* **26,** 1321–1324.

Tsumura, N., A. Hasegawa, and S. Horiuchi (1996). Simultaneous estimation of attenuation structure, source parameters, and site response spectra: application to the northeastern part of Honshu, Japan, *Phys. Earth Planet. Interiors* **93,** 105–121.

Winkler, K. W., and A. Nur (1979). Pore fluids and seismic attenuation in rocks, *Geophys. Res. Lett.* **6,** 1–4.

Winkler, K. W., and A. Nur (1982). Seismic attenuation: effects of pore fluids and frictional sliding, *Geophys.* **47,** 1–15.

Department of Geology and Geophysics
University of Wisconsin–Madison
Madison, Wisconsin 53706

Manuscript received 30 July 2003.